Mapping surface displacement using a pair of interferograms: comparative study

Stéphanie Dumont[1,2,3,*], Fernando Lopes[4], Freysteinn Sigmundsson[1], Vincent Drouin[1,5]

[1]Nordic Volcanological Center, Institute of Earth Sciences, University of Iceland, Reykjavik, Iceland;

[2] University of Beira Interior, Covilhã, Portugal;

[3] Instituto Dom Luiz (IDL), Faculdade de Ciências, Universidade de Lisboa, Lisboa, Portugal;

[4]Institut de Physique du Globe de Paris, Paris, France

[5]Iceland GeoSurvey, Iceland;

[*]Corresponding author's email: sdumont@segal.ubi.pt

Abstract

Interferometric analysis of Synthetic Aperture Radar satellite images (InSAR) measures only one component of ground deformation, in the satellite line-of-sight direction. In order to fully resolve the three dimensional (3D) ground displacement field, InSAR images acquired with different imaging geometries are required. Despite the increase in the number of SAR missions, an area is most frequently imaged by an InSAR pair, one image from an ascending and another from a descending satellite track, with difference in the incidence angle allowing only partial retrieval of a 3D surface deformation field. In particular, the near-polar orbits of SAR satellites do not allow good retrieval of the north component of displacement. Here we use a model resolution matrix approach for an InSAR pair to quantify the ability to reconstruct the three components of the deformation field. We present and compare the results of the decomposition for three methods, including two widely used techniques and ours that is based on the Singular Value Decomposition (SVD) algorithm. The study case for the comparative analysis is focussed on Bárdarbunga volcano area (central Iceland) and complementary tests and modelling are performed using synthetic data. We discuss the retrieved east and vertical components for each decomposition method in terms of approach, viewing geometry, nature and orientation of the deformation field allowing us to suggest some recommendations when planning the use of a decomposition method.

Keywords: Interferometric Synthetic Aperture Radar (InSAR); Surface deformation; Singular Value Decomposition; InSAR pair; Line-Of-Sight (LOS); Two-dimensional (2D) displacements; Bárdarbunga

1 Introduction

Interferometric analysis of synthetic aperture radar (InSAR) images acquired by satellites have improved our understanding of ground deformation since the 1990s. It has become an inescapable tool for mapping and monitoring a wide range of deformation processes, including studies in remote areas of most difficult access where ground-based surveys can be hardly envisaged ([Gabriel et al., 1989]; [Massonnet and Feigl, 1998]). InSAR techniques allow to detect mm to cm scale ground movements over wide areas (up to several 100 km for wide swath) whatever the light or the weather conditions. In particular, they have been used to monitor volcanic processes ([Vilardo et al., 2010]; [Pinel et al., 2014]; [Chaussard, 2016]; [Hutchison et al., 2016]; [Dumont et al., 2018]), faulting and earthquakes ([Fialko et al., 2001]; [Wang et al., 2014]; [ElGharbawi and Tamura, 2015]; [Dumont et al., 2016]), subsiding areas due to groundwater extraction ([Bell et al., 2008]; [Keiding et al., 2010]; [Chaussard et al., 2014]), glacier movement ([Joughin et al., 1998]; [Kumar et al., 2011]) or landslides ([Tong and Schmidt, 2016]; [Sun et al., 2017]; [Béjar-Pizarro et al., 2017]).

The characterization of ground deformation in the three dimensions (3D) of space is of crucial importance for deciphering the nature and the dynamics of the deformation source. However, a single interferogram provides only one dimensional measurement consisting in a projection of the surface deformation field onto the line-of-sight (LOS). In order to fully resolve the 3D deformation field using classical InSAR techniques, e.g. based on the along line-of-sight phase difference, a combination of at least three interferograms acquired with different imaging geometries is required ([Massonnet and Feigl, 1998]; [Hanssen, 2001]; [Froger et al., 2004]; [Wright et al., 2004]; [Hu et al., 2014]). Despite the increase in the number of satellites carrying SAR sensors since the 1990's, it is, however, uncommon to have three or more scenes acquired with significantly different geometries covering the same area for the same time-span. It is more common to routinely acquire images from two different views or a pair of interferograms, e.g. from ascending and descending orbits, what nevertheless prevents the full retrieval of the 3D deformation field. The decomposition of interferogram pairs has thus become more and more frequent, providing high resolution measures of the vertical and horizontal deformation over very large areas that can easily be compared with other data sets. With the new generations of satellites such COSMO-SkyMed (CSK), TerraSAR-X (TSX), ALOS-2 or Sentinel-1, the acquisition modes have been made more and more flexible especially with larger ranges of incidence angles offering new possibilities of combinations. Our study focuses on these combinations of InSAR data although other approaches exist as for instance, the processing of along-track interferograms [Bechor and Zebker, 2006] or the combination of interferograms with other data sets such GNSS measurements ([Gudmundsson et al., 2002]; [Wang et al., 2012]; [Pagli et al., 2014]; [Jo et al., 2015]) and may be used to solve the 3D deformation field.

The plane defined by the two incidence angles of the ascending and descending configurations is called the "co-plane" (Fig.1) and includes the LOS changes detected in the interferograms [Ozawa and Ueda, 2011]. The movements detected in the LOS can thus be expressed by two components in this co-plane which is close to being an east-west oriented vertical plane (Fig. 1). The vertical and east components can therefore be reconstructed with a relatively good accuracy from an InSAR pair while the north component of the displacement field is only to a minor degree included in this co-plane and consequently poorly resolved in general ([Fujiwara et al., 2000]; [Ozawa and Ueda, 2011]). In polar regions the satellite orbit configuration is, however, such that some sensitivity with respect to the north-south direction can be reconstructed [Ozawa and Ueda, 2011].

With this paper, we start by quantifying our capacity to retrieve the components of the 3D displacement field using an InSAR pair and the model resolution matrix. This latter can be seen as a measurement of the uncertainties with respect to the true deformation field we do not measure using SAR sensors. The Singular Value Decomposition or SVD, we then present, allows to condition the underdetermined system composed of the pair of interferograms and whose inversion allows the retrieval of the east and vertical components. This approach is compared to two other techniques classically used to solve the non-invertible system formed by a pair of interferograms, and for this, real and simulated data sets are considered. The real example is taken from a recent active volcano-tectonic event in Iceland, that was associated with two different surface processes that have been well characterized ([Sigmundsson et al., 2015]; [Gudmundsson et al., 2016]). Finally, we conclude by revisiting the classical modelling approach by using decomposition methods on synthetic interferograms.

2 Data

2.1 Study site

Our study case takes place in central Iceland along the Eastern Volcanic Zone and nearby the north-west corner of the Vatnajökull glacier (Fig. 2a). On 16 August 2014, a segmented dyke began propagating from Bárdarbunga ice-capped caldera. Over two weeks, the eight main dyke segments formed over a distance of 50 km (Fig. 2b). Inversion of geodetic measurements revealed an opening of 4-6 m in its last segment ([Sigmundsson et al., 2015]; [Ruch et al., 2016]; [Heimisson and Segall, 2020]). The dyke feeded a major fissure eruption at its far end over 6 months, ending 26 February 2015 [Pedersen et al., 2017]. Simultaneously to the dyke emplacement, a slow caldera collapse initiated resulting from the magma

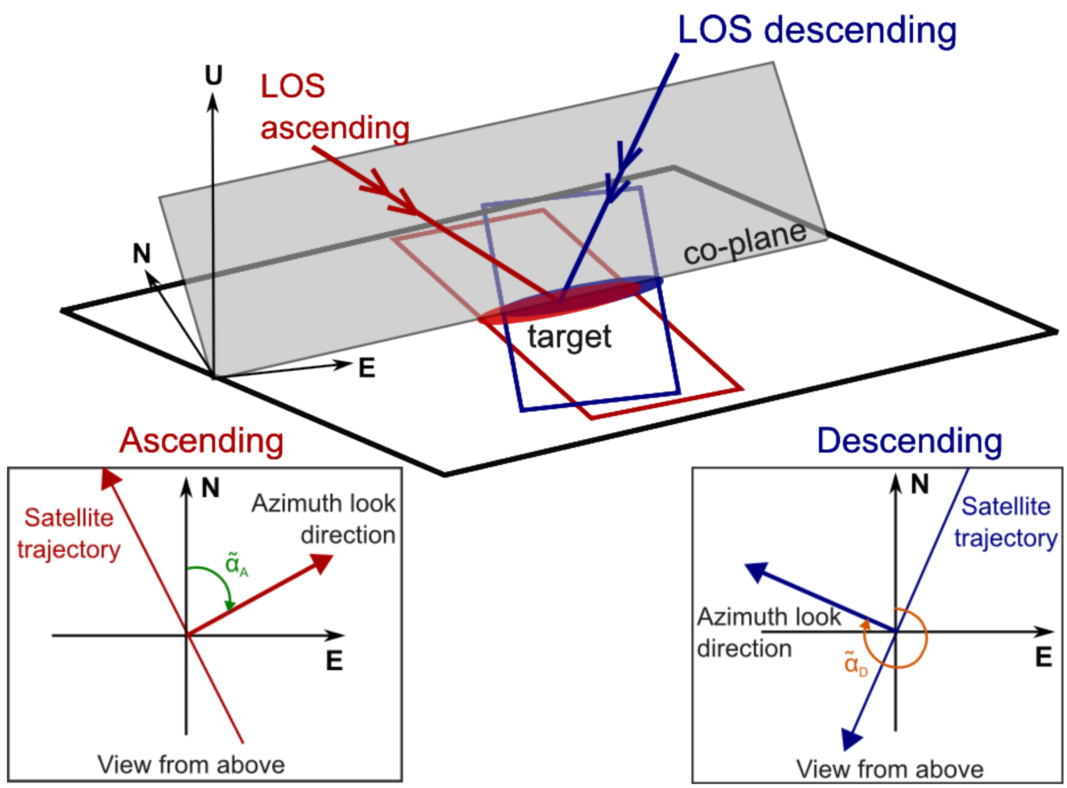

Figure 1. Imaging geometry of an InSAR pair for a right-looking SAR satellite. The ascending LOS and the corresponding track on the ground are shown in red and the descending ones in blue. In the case shown, the two LOS have different incidence angles with the angle for the ascending track being more oblique than the one for the descending track. The ascending and descending LOS directions define a common plane where the displacement components can be expressed. The two boxes show a horizontal plan (view from above), with the azimuth look angle for the descending and ascending geometries. U, N and E represent the Up, North and East geographical directions.

source deflation [Parks et al., 2017]. It resulted in a 65-m deep collapse at the ice-capped volcano at the end of the eruption ([Gudmundsson et al., 2016]; [Coppola et al., 2017]).

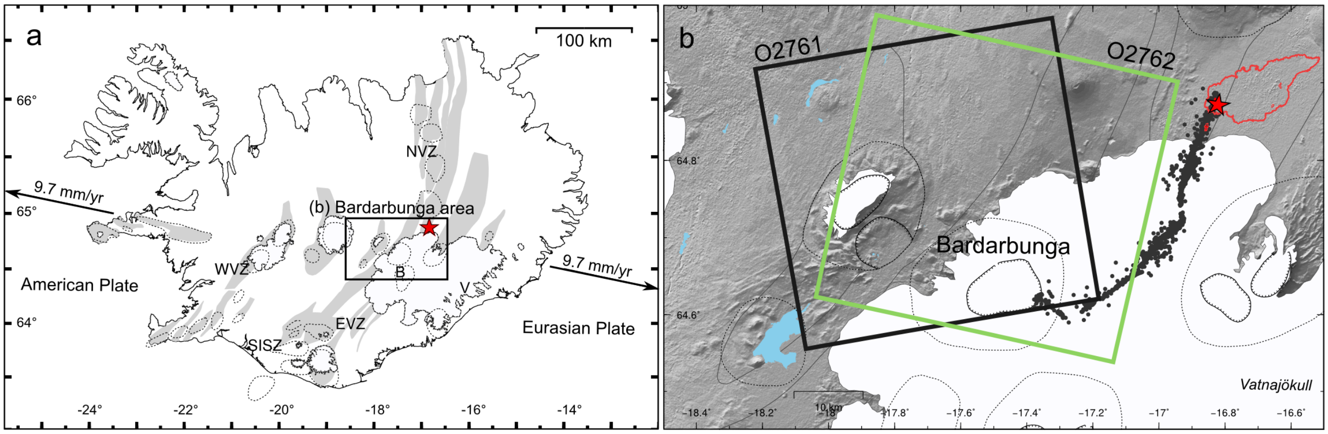

Figure 2. (a) Volcano-tectonic map of Iceland including the Bárdarbunga area. Background map shows the Eastern Volcanic Zone (EVZ), the Western Volcanic Zone (WVZ), the Northern Volcanic Zone (NVZ) and the South Iceland Seismic Zone (SISZ), with fissure swarms (shaded) and central volcanoes (dotted outlines). After [Johannesson and Saemundsson, 2009]. Outlines of icecaps are also shown. Vatnajökull icecap is marked with a V and Bárdarbunga central volcano with a B. Boxe indicates the studied area shown in (b). (b) Map of the NW-Vatnajökull area, including the Bárdarbunga volcano with seismicity (gray dots) over the dyke path. The eruption site opened at the dyke tip (red star), and fed an extensive lava field over 6 months shown with the red outlines. After [Sigmundsson et al., 2015].

2.2 SAR data and processing

Iceland has been granted by the Committee on Earth Observation Satellites (CEOS) through the Icelandic Volcanoes Supersite project as Permanent Geohazard Supersite since late 2013 allowing regular acquisitions over all active volcano-tectonic regions of the island by different satellite SAR sensors [Dumont et al., 2018]. In Iceland, SAR satellite images for InSAR applications have preferentially been acquired and used during summer thawing season, ∼June to August-September as Icelandic ground is seasonally frozen [Oelke and Zhang, 2004]. The limited vegetation and acquisitions during summer period allow to maintain a good coherence over the scenes, up to several years even using X-band data, e.g. [Drouin et al., 2017] (Supplementary Material, Fig. S1).
Here we use COSMO-SKyMed (CSK) SAR images whose wavelength is 3.12 cm and whose characteristics are presented in Table 1. We use the term "oblique" for designating incidence angles $\geq 30°$ as those of CSK data, "high" for sub-vertical ones, e.g. $< 30°$ and "mixed" for a combination of high and

oblique incidence angles. The two interferograms formed cover both 36 days although they are shifted by one day. We therefore assume that the two interferograms capture the same deformation. Their LOS unit vectors are $(-0.66, -0.23, 0.71)$ and $(0.55, -0.20, 0.81)$ in east, north and vertical components, for the ascending and descending orbits respectively. For this example, the look vectors are about constant across the scene.

Table 1. Details of the COSMO-SkyMed (CSK) interferograms used in this study.

	Ascending	Descending
Orbit	2761	2762
Dates	20140811-20140916	20140810-20140915
B_p (m)	77	279
Mean incidence angle	44.56	35.67
Heading	-19.47	-160.30
Look direction	70.53	-70.3

CSK data were processed using the InSAR Scientific Community ENvironment (ISCE) software ([Rosen et al., 2012]). The InSAR processing steps included co-registration of the SLC images, interferogram formation and flattening, correlation calculation, removal of topographic phase, filtering, phase unwrapping and geocoding. For both ascending and descending configurations, the SLC images were multi-looked to reduce the speckle effect, 12 x 6 in range and azimuth directions respectively, producing square ground pixels of $\sim$15 x 15 m. The DEM used for removing topographic fringes in Bárdarbunga area is a mosaic DEM mostly composed by TanDEM-X intermediate DEM, whose gaps were filled using DEM from the ASTER satellite mission and the EMISAR DEM [Magnússon et al., 2005], the pixel size for this DEM being $\sim$10 x 10 m. Interferograms were filtered using a power spectrum filter [Goldstein and Werner, 1998] and were unwrapped using the statistical-cost, network-flow based algorithm, Snaphu [Chen and Zebker, 2002]. The unwrapped phase map was then converted to displacements with a final geocoded resolution similar to that of the DEM.

The reference point for the ascending interferogram was taken in the south-west area, where the displacement was relatively limited but not null (Supplementary Material, Fig. S2). For this reason, we calibrated the reference point using HSKE GNSS station as it detected only $\sim$2 cm of surface deformation during the 36 days interval studied. As HSKE being a few hundred meters off the interferogram, we assumed the reference point located further 2.9 km, e.g. [-18.0364; 64.6320], to have recorded similar deformation (Supplementary Material, Fig. S2). More, the last measurement at this campaign site was performed on 12th September, e.g. four days prior to the second SAR ascending acquisition. However, as the daily movement at the station has not exceed 3 mm since 30th August [Sigmundsson et al., 2015], the difference of displacement between the 12 and 16 September is of uncertainty order. The reference point value was calculated by an average displacement using a 3×3 window and compared to GNSS data, once projected into the LOS. For the descending interferogram, we applied a similar approach with a point located at 2.5 km from the HSKE GNSS station, e.g. [-18.0330 ; 64.6251].

The descending interferogram shows an orbital ramp (Supplementary Material, Fig. S2) which was removed using a linear ramp excluding the deforming area (Supplementary Material, Figs. S2 and S3). We also investigated the atmospheric contribution in both interferograms by evaluating the correlation between the phase and the topography [Cavalié et al., 2008] along the northern side of Tungnafellsjökull glacier (Supplementary Material, Figs. S2 and S3). The linear phase change correlated with elevation was only removed for the descending interferogram (Supplementary Material, Figs. S3 and S4).

3 Methodology

3.1 Previous methods for retrieving displacements from an InSAR pair

Measurements of the satellite-to-Earth-surface range changes, denoted d_{LOS}, consist in the projection of the 3D surface displacement field $\overrightarrow{U}$ onto the satellite LOS direction. It is given by [Hanssen, 2001] as

$$d_{LOS} = -\overrightarrow{L}.\overrightarrow{U} \tag{1}$$

where $\overrightarrow{L}$ is the unit vector pointing from the ground to the satellite. Here $\overrightarrow{U} = [U_e, U_n, U_{up}]$ where U_e, U_n and U_{up} are the east, north and vertical displacement components, respectively.

The two different lines of sight, ascending ($\tilde{\alpha_A}$) and descending ($\tilde{\alpha_D}$) combined for the decomposition, have to cover as best as possible the same time interval such the ground deformation captured in between the acquisition dates is the same. Similarly, such combination assumes that atmospheric conditions are negligible or the same on all four dates. With such an InSAR pair, the following system of linear equations applies:

$$\begin{pmatrix} d_{ASC} \\ d_{DESC} \end{pmatrix} = \begin{pmatrix} -\sin(\theta_A)\sin(\tilde{\alpha}_A) & -\sin(\theta_A)\cos(\tilde{\alpha}_A) & \cos(\theta_A) \\ -\sin(\theta_D)\sin(\tilde{\alpha}_D) & -\sin(\theta_D)\cos(\tilde{\alpha}_D) & \cos(\theta_D) \end{pmatrix} \begin{pmatrix} U_e \\ U_n \\ U_{up} \end{pmatrix} \tag{2}$$

where θ is the incidence angle, $\tilde{\alpha}_A$ and $\tilde{\alpha}_D$ are the azimuth look directions for the ascending and descending passes respectively, and a right-looking satellite. Both azimuth look directions are equal to $\alpha_H - 3\pi/2$ where α_H corresponds to the satellite heading defined as the direction of local azimuth on the ground surface, measured clockwise from north (Fig. 1). For a left-looking satellite, $\tilde{\alpha}_A$ and $\tilde{\alpha}_D$

would be equal to $\alpha_H - \pi/2$. This system, with more unknown parameters (U_e, U_n, U_{up}) than data (d_{ASC} and d_{DESC}) is under-determined with a non-unique solution, this is why different approaches have been developed to derive an estimate of the east and vertical components.

A first approach consists in assuming the nature of the ground deformation leading to the elimination of one or two of the horizontal components. If one of three displacement components is assumed to be zero (e.g. U_n equal zero), then the 2x3 matrix in Eq. (2) reduces to a 2x2 matrix and the equations to solve become well determined. We refer to this approach as the two-component linear inversion. For examples of use of this approach see [Joughin et al., 1998]; [Manzo et al., 2006]; [Bell et al., 2008]; [Samieie-Esfahany et al., 2009]; [Kumar et al., 2011]; [Ozawa and Ueda, 2011]; [Wang et al., 2012]; [Rucci et al., 2013]; [Chaussard et al., 2013]; [Chaussard et al., 2014]; [Samsonov et al., 2014], [Chaussard, 2016]; [Dumont et al., 2016]; [Hutchison et al., 2016]; [Parker et al., 2016]; [Wittmann et al., 2017], [Drouin and Sigmundsson, 2019] and [Wang et al., 2019]. However, such assumption necessarily affects the inferred value of the two remaining components considering the total displacement detected in the LOS is still the same. Nonetheless, as the SAR satellites are operated along near-polar orbits, the north-south component cannot be well resolved as previously explained. Its removal should therefore have a minimal impact, in particular if the real north-south ground motion is small. Ignoring the two horizontal components and assuming purely vertical displacement field will necessarily lead to an over- or underestimate of the vertical component depending on the LOS direction with respect to the true horizontal deformation [Samieie-Esfahany et al., 2009].

Another approach to solve Eq. (2) is to consider linear combinations of the observed LOS changes using the different LOS unit vectors (the LC method). Simple linear combinations of ascending and descending interferograms aim at reducing the sensitivity of two of the three displacement components. For examples, see [Fujiwara et al., 2000]; [Lundgren et al., 2004]; [Casu et al., 2006]; [Keiding et al., 2010]; [De Zeeuw-van Dalfsen et al., 2012]. Such linear combinations have usually been applied to SAR data sets for which the absolute value of the incidence angles are very similar ($\mid \theta_A \mid \simeq \mid \theta_D \mid = \theta$) as for example, those fixed for the satellites ERS-1 and 2. More, the heading of the ascending and descending configurations, and therefore the azimuth look directions are also supposed very close in terms of absolute value: $\tilde{\alpha}_D = -\tilde{\alpha}_A \rightarrow \mid \tilde{\alpha}_D \mid = \mid \tilde{\alpha}_A \mid = \alpha$. The near-vertical ($n_U$) component of deformation is usually calculated by adding together the descending and ascending LOS changes, and the near-east (n_E) component by subtracting the ascending from the descending one. Using the two hypothesis above-mentioned, the near-vertical and near-east components can be expressed as follow:

$$n_U = \frac{d_{ASC} + d_{DESC}}{2\cos\theta} + \tan\theta\cos\alpha U_n \qquad n_E = \frac{d_{ASC} - d_{DESC}}{2\sin\theta\sin\alpha} \tag{3}$$

These operations are also applied to the unit vectors associated with each interferogram, as illustrated later in section 4, quantifying somehow how sensitive are n_U and n_E to the three displacement components. The sensitivity vectors thus obtained are then normalized using the highest value of the sensitivity vectors. However, the formulations of Eq. 3 show that n_E is described independently from the other displacement components, while n_U does still include a small contribution of U_n according to the two hypothesis above-mentioned. These two ways to proceed reveal some discrepancies, that are more pronounced when the hypothesis, in particular that related to incidence angles, are only roughly approximated.

3.2 The model resolution matrix approach

As for other geophysical measurements, the reconstruction accuracy of the true unknowns, in our case the three displacement components, is completely governed by the data acquisition geometry as shown by Eq. 2. As the acquisition system does not allow to measure the true ground deformation field, it acts as a filter. In order to estimate the impact of the geometry of acquisition on the model parameters and therefore to have a quantitative idea of the filter impact on the reconstructed displacement, one can evaluate the model resolution matrix of the problem. The linear forward problem in Eq. (2) takes the following form,

$$\mathbf{d} = \mathbf{G}\mathbf{m} \tag{4}$$

where **d** is the data vector and **m** the model vector. In our case **d** are the InSAR ascending and descending LOS changes and **m** the 3D displacement field. The link between the data and the model is a linear operator **G**, the 2 x 3 matrix in Eq. (2). It represents a transformation matrix that contains only information on the geometry of acquisition. The pair of interferograms forming an under-determined system, we adopt the minimum length solution [Menke, 2018]. The minimum length solution is particularly well appropriate when working on surface displacements as deformation processes are physical and natural processes associated with Earth system whose total entropy is minimized from a thermodynamic perspective. In that case, the general inverse $\mathbf{G}^{-g}$ for an under-determined system has been given and fully described by [Menke, 2018], such:

$$\mathbf{G}^{-g} = \mathbf{G}^T[\mathbf{G}\mathbf{G}^T]^{-1} \tag{5}$$

An estimate of the model parameters, $\mathbf{m}^{est}$, can therefore be written such: $\mathbf{m}^{est} = \mathbf{G}^{-g}\mathbf{d}^{obs}$. As we previously mentioned, we can wonder how far is the estimated solution ($\mathbf{m}^{est}$) from the true solution ($\mathbf{m}^{true}$), e.g the components of the true deformation field. If all model parameters would have been independently predicted or resolved, we could have written: $\mathbf{G}\mathbf{m}^{true} = \mathbf{d}^{obs}$, which is not possible because of the SAR configuration. $\mathbf{m}^{est}$ can thus be expressed such:

$$\mathbf{m}^{est} = \mathbf{G}^{-g}\mathbf{d}^{obs} = \mathbf{G}^{-g}[\mathbf{G}\mathbf{m}^{true}] = [\mathbf{G}^{-g}\mathbf{G}]\mathbf{m}^{true} = \mathbf{R}\mathbf{m}^{true} \tag{6}$$

$\mathbf{R}$ represents the model resolution matrix and allows to know whether the model parameters can be independently predicted while the estimates of the model parameters ($\mathbf{m}^{est}$) represent weighted averages of the true model parameters. When $\mathbf{R}$ gets closer to the identity matrix, the estimates of the model parameters are closer to the real components of the deformation field. In the framework of an under-determined system solved using the minimum length solution [Menke, 2018], $\mathbf{R}$ can be expressed as follow:

$$\mathbf{R} = \mathbf{G}^{-g}\mathbf{G} = \mathbf{G}^T[\mathbf{G}\mathbf{G}^T]^{-1}\mathbf{G} \tag{7}$$

With the acquisition geometry of SAR satellites, $\mathbf{R}$ is different from the identity matrix, as illustrated with the model resolution matrices represented in Figure 3. With the model resolution matrix approach, one can quantify how each real component (U_e, U_n and U_{up}) contributes to reconstruction of the deformation field observed by two complementary near-polar tracks. As illustrated in Figure 3a for the Bárdarbunga area, the reconstructed value of U_{up} (U^*_{up}), for example, can be written:

$$U^*_{up} = 0.0139U_e - 0.2576U_n + 0.9283U_{up} \tag{8}$$

The reconstructed vertical component includes 93.0% of the true vertical displacement and additionally 25.8% of the true north displacement and 1.4% of the true east displacement. The reconstructed east component, U^*_e, includes 1.4% of the true vertical, 5.0% of the true north displacement and 99.7% of the true east. Similarly, the reconstructed north component (U^*_n) is composed by 25.8% of the true vertical component, 7.4% of the true north component and 5.0% of the true east component. Figure 3 reveals that except for U^*_n, the true north component U_n appears systematically as the second minor contribution. This contribution to both U^*_{up} and U^*_e increases with more oblique incidence angles, even if it is more pronounced for U^*_{up}. This trend is also accompanied by a relative decrease, a few percent ($< 10\%$), of the U_{up} contribution to U^*_{up} while the reconstruction of U^*_e is almost not sensitive to the increase of the obliquity of the combined incidence angles. Finally the model resolution matrix shows that only two components, U^*_{up} and U^*_e can be almost fully retrieved whereas it is not possible to retrieve the north component for SAR sensor configurations (Fig. 3). Indeed, the acquisition geometry imposes that the most significant part of the reconstructed north component corresponds to the true vertical component and not the true north component. These examples illustrate well how the north component is seen by the acquisition geometry of two complementary tracks and why it can not be further considered. The model resolution matrix can be viewed as representing uncertainties of the estimated reconstructed components with respect to the true deformation field.

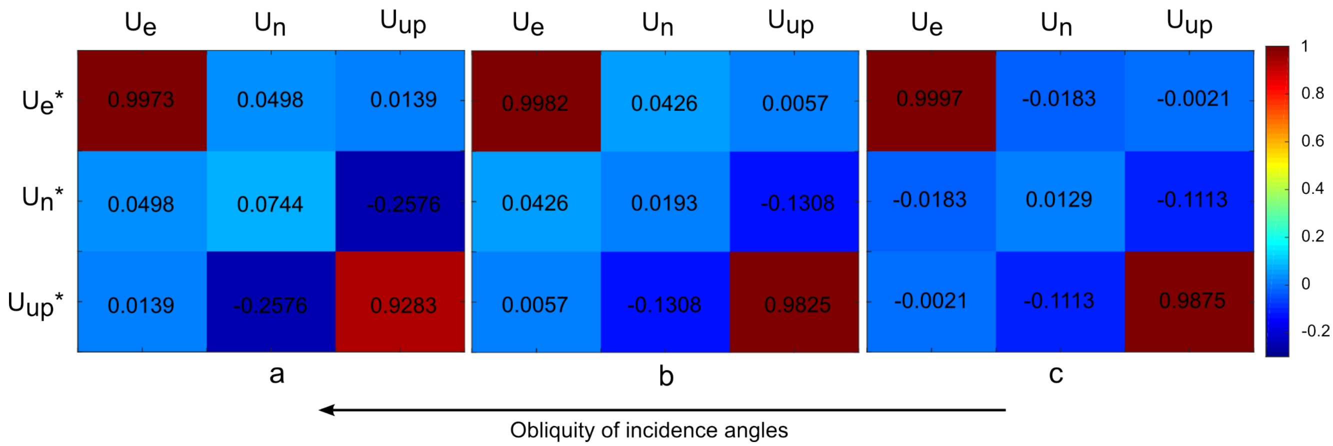

Figure 3. Model resolution matrices for three geometries of satellite SAR acquisition. (U_e^*, U_n^* and U_{up}^*) correspond to the reconstructed east, north and up components respectively of the displacement field whereas the (U_e, U_n and U_{up}) define the real deformation field. The model resolution matrix for the Bárdarbunga area is presented in (a), representing a combination of two oblique incidence angles (see Table 1 and Section 2.2). (b) Model resolution matrix for a combination of low and high incidence angles, later called mixed incidences angles. Example taken from TerraSAR-X data over Reykjanes Peninsula accessible from the Iceland Volcanoes Geohazard Supersite [Parks et al., 2018]. The related unit vectors are (-0.66 -0.13 0.73) and (0.39 -0.10 0.91) for the ascending and descending passes in the east, north and vertical components respectively. (c) Model resolution matrix for a combination of two high incidence angles, estimated for ERS/Envisat SAR data from [Keiding et al., 2010]. The related unit vectors are (-0.32 -0.10 0.94) and (0.40 -0.11 0.91) for the ascending and descending passes in the east, north and vertical components respectively. The model resolution matrix shows how the vertical and east components are almost fully retrieved with better resolution for high or mixed incidence angles.

3.3 The SVD as natural inversion solution

The linear system described in Eq. (2) is under-determined with $\mathbf{G}$ being an ill-conditioned matrix with more columns than rows, it is therefore non invertible in this form. Singular Value Decomposition (SVD) is a classical method used to construct $\mathbf{G}^{-g}$ [Menke, 2018]. We therefore propose to use it for jointly inverting d_{ASC} and d_{DESC} (Eq. 2).
$\mathbf{G}$ might be written as a product of three matrices, $\mathbf{U}\ \mathbf{\Lambda}\ \mathbf{V}^T$, with $\mathbf{U}$ and $\mathbf{V}$, two square matrices of eigenvectors and a diagonal, non-square matrix composed of eigenvalues $\mathbf{\Lambda}$ [Golub and Kahan, 1965]. This 2 x 3 matrix of eigenvalues $\mathbf{\Lambda}$ is arranged such that the eigenvalues are in order of decreasing size with some of them that may be null. $\mathbf{\Lambda}$ can be partitioned such the non-zero eigenvalues can be gathered

into the submatrix $\mathbf{\Lambda}_p$ [Menke, 2018]:

$$\mathbf{\Lambda} = \begin{pmatrix} \mathbf{\Lambda}_p & 0 \\ 0 & 0 \end{pmatrix} \tag{9}$$

As the null eigenvalues do not provide any information, a truncation of $\mathbf{\Lambda}$ can thus be performed without altering the information initially contained in $\mathbf{G}$ ([Hansen et al., 1992]; [Menke, 2018]). In our case, this step consists in deleting the third column that makes $\mathbf{\Lambda}$ a 2 x 2 matrix. The inversion is then calculated using the pseudo truncated inverse of $\mathbf{G}$ such: $\mathbf{G}^{-g} = \mathbf{V}_p \mathbf{\Lambda}_p^{-1} \mathbf{U}_p^T$.
The corresponding model resolution matrix is given by: $\mathbf{R} = \mathbf{G}^{-g}\mathbf{G} = [\mathbf{V}_p \mathbf{\Lambda}_p^{-1} \mathbf{U}_p^T][\mathbf{U}_p \mathbf{\Lambda}_p \mathbf{V}_p^T]$. In addition to allow the inversion of our under-determined system (Eq. 2), the SVD algorithm does not modify the initial system that we aim at solving (Eq. 2). This inversion process can be easily implemented using *pinv* function in the Octave GNU software, which also exists in Matlab. We call this method "truncated SVD" in the following text.

4 Results

4.1 Interferograms

The two interferograms formed over Bárdarbunga area show apparent reverse surface displacements from ascending and descending viewing geometries suggesting a significant horizontal component (Fig. 4). The ascending interferogram shows an increase in the satellite-target distance of $\sim$ 20 cm on the western part of the ice-covered Bárdarbunga caldera. This distance change exceeds 25 cm in between some of the glacier tongues. On the north-eastern side of the scene, this distance is shortened by $\sim$40 cm. On the descending interferogram, a reduction in the LOS distance change is detected in the caldera vicinity with a maximum about 15-20 cm and whose pattern extends up to Vonaskard caldera, located further west. A lengthening superior to 20 cm is also observed north-east of the scene.
These two interferograms captured two different processes involving horizontal movements. The first one took place outside the icecap edge next to the Bárdarbunga caldera and corresponds to a subsidence induced by the withdrawal of the magma reservoir located below Bárdarbunga caldera ([Riel et al., 2015]; [Gudmundsson et al., 2016]; [Coppola et al., 2017]; [Parks et al., 2017]). The second one detected on the north-east corner of the scenes, corresponds to an uplift caused by the dyke emplacement over a distance of 50 km mostly below Vatnajökull glacier and emitted from Bárdarbunga volcano ([Sigmundsson et al., 2015]; [Ruch et al., 2016]; [Heimisson and Segall, 2020]).

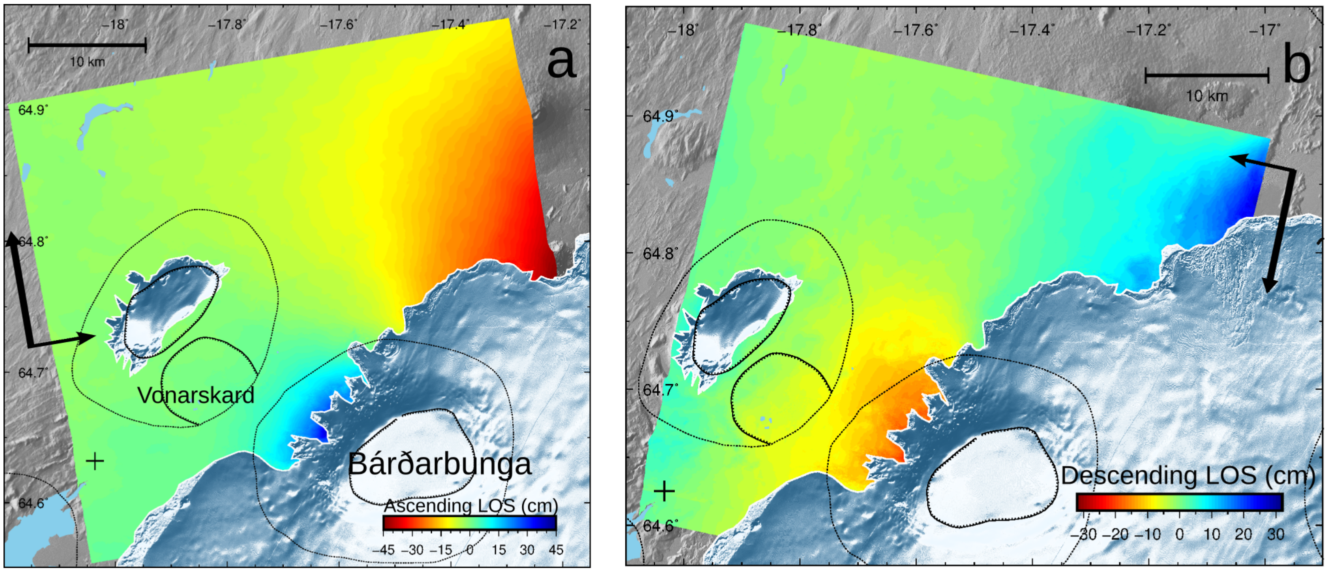

Figure 4. Surface displacements in the NW-Vatnajökull area captured by InSAR. LOS displacement maps acquired along ascending (a) and descending (b) passes spanning almost the same time interval, from 11 August to 16 September 2014 for the ascending configuration and from 10 August to 15 September 2014 for the descending one. The large arrows show the satellite flight directions and the small ones the look direction from the satellite to the ground. See Section 2.2 and Appendixe A for more details on the data processing.

4.2 Inversion results and comparison with other decomposition methods

In this section, we compare the results obtained using the three decomposition methods including ours. As the two inversion-based decomposition methods have been previously described, we start by quickly introducing the LC method.
The sensitivity vectors for the near-up (n_U) and near-east (n_E) are estimated by summing and substracting, respectively the ascending and descending LOS unit vectors (see Section 3.1), illustrated below with Equations 10 and 11 for Bárdarbunga area. The normalization factor for the component of interest corresponds to the highest value of the sensitivity vector. It is used to normalize the sum and difference of the descending and ascending LOS changes that is of 1.52 for n_U and 1.21 for n_E (Equations 10 and 11).

The LC method applied to CSK data over Bárdarbunga area gives:

$$n_U = \frac{1}{1.52}(d_{ASC} + d_{DESC}) = \frac{1}{1.52}(-0.11, -0.42, 1.52)(U_e, U_n, U_{up})^T \tag{10}$$

$$n_E = \frac{1}{1.21}(d_{DESC} - d_{ASC}) = \frac{1}{1.21}(1.21, 0.04, 0.10)(U_e, U_n, U_{up})^T \tag{11}$$

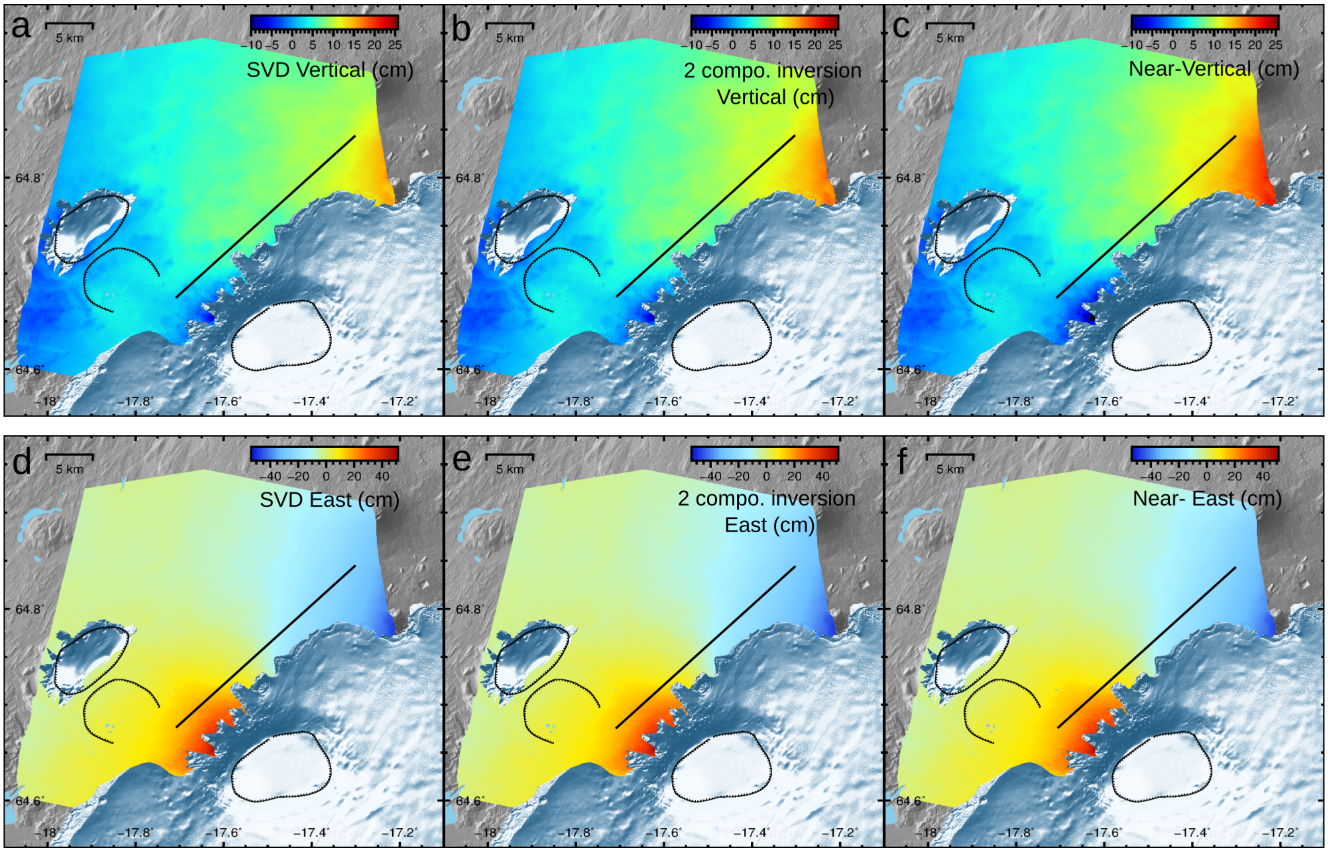

Figure 5. Reconstructed components of the displacement field. (a-c) Vertical and (d-f) east components resulting from the truncated SVD approach (a and d), two-component linear inversion (b and e) and the LC method (c and f). Black lines indicate locations of profiles shown in Figure 6.

Retrieved vertical and east components of the deformation field are shown in Figures 5a–c and 5d–f respectively, for all three decomposition methods. The upper and lower panels clearly reveal that the largest displacements are detected along the east-west direction. The spatial distribution and amplitudes obtained for each reconstructed east component, are very similar (Fig. 5d–f), what is also illustrated with the profiles and their differences that do not exceed $\sim$1 cm (Fig. 6). The eastward movement in the vicinity of Bárdarbunga caldera exceeds 30 cm in between some glacier tongues. Further north-east, the westward movement induced by the dyke opening is mostly of 20-25 cm. More discrepancies appear in the reconstruction of the vertical component (Figs. 5a–c and 6). As an example, the subsidence detected on the western part of Bárdarbunga caldera extends more with the LC method with the highest estimates ($\geq$ 10 cm). On the contrary, the SVD approach results in a more limited subsiding area that reaches up to

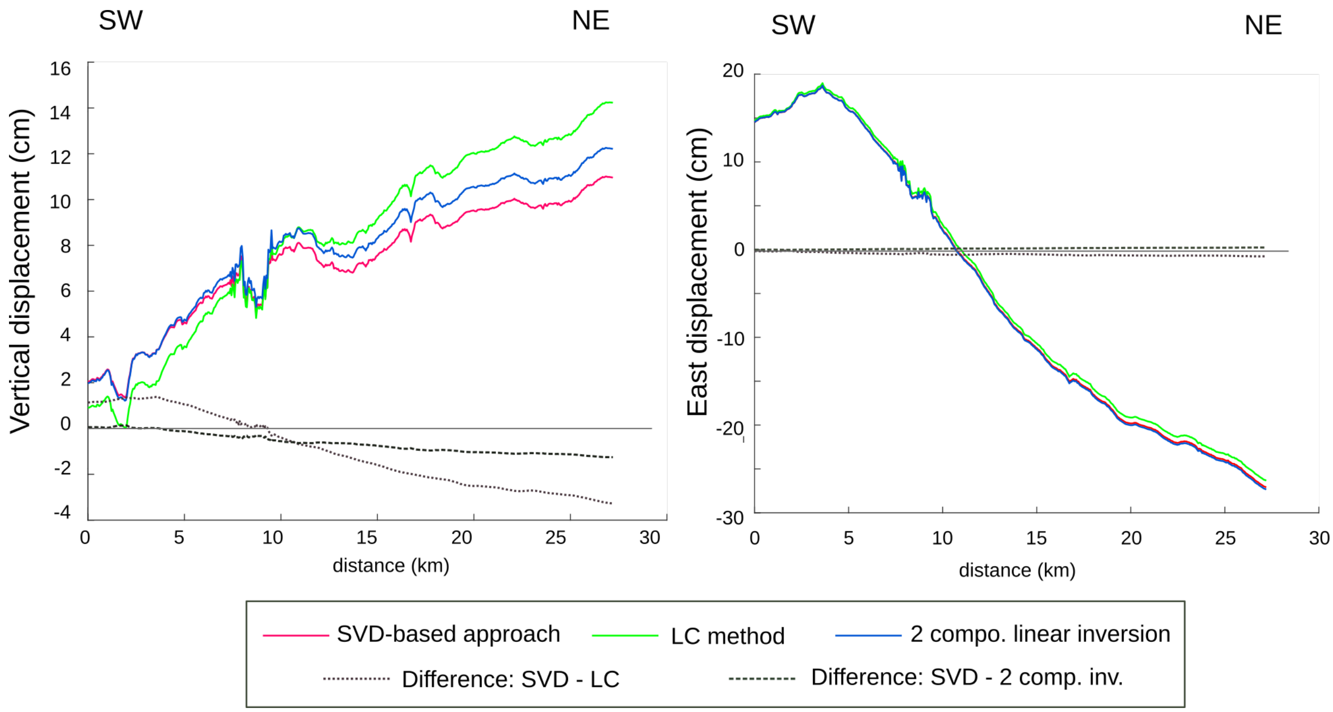

Figure 6. Comparative analysis of the three decomposition methods using profiles and the example of Bárdarbunga area. The profiles are extracted from the reconstructed vertical (left column) and east components (right column). They are shown for the truncated SVD (red), the two-component linear inversion (blue), and the LC method (green); see text for more details. The dark-grey dotted curves represent the difference between the SVD and LC methods, and the dashed one the difference between the SVD and 2 compo. linear inversion methods. Profile locations are indicated in Figure 5.

5-10 cm at maximum. Results from the two-component linear inversion appear as intermediate to both previous methods. In the sector of the dyke, highest uplift values are also obtained for the LC method. This latter approach shows actually the highest range of values for U^*_{up} while our SVD-based approach shows the smallest range. This observation is reinforced by the analysis of the profiles (Fig. 6). This figure shows that the SVD-based and two-component linear inversions result in very similar estimates of U^*_{up} in the subsiding area; estimates whose differences increase towards the north-east, to reach $\sim$1 cm at the end of the profile. This is also where the differences between the methods are stronger in both U^*_{up} and U^*_{e} (Fig. 6). This comparison suggests that when horizontal deformation takes predominance over the vertical one as in the area affected by dyke-induced deformation, the differences between the three approaches are more pronounced for reconstructing the vertical and even the east components.

4.3 Further analysis of decomposition methods using synthetic data

The three methods used for decomposing a pair of two interferograms can be further compared with synthetic data. Here we: (1) decompose two interferograms whose acquisition geometries are known as well as the true deformation field, and (2) use the decomposition results to model the deformation field.

4.3.1 How decomposition methods do influence results?

First, we consider a 3D surface displacement field created by a point source of pressure within an elastic half-space known as the Mogi model [Mogi, 1958]. Our source is located at 4 km depth and associated with a volume change dV of 0.1 km^3. The resulting deformation field (Fig. 7a, first column) is projected into the LOS using the acquisition geometry of CSK SAR data presented in Table 1 (both incidence angles are very obliques with a difference of $\backsim 10°$). We then reconstruct the components of the displacement field using the three decomposition methods (Fig. 7a, columns 2-4).

Figures 7 and S5 (Supplementary Material) reveal how U_e^* is better reconstructed whatever the decomposition methods used than U_{up}^*. For the two-component linear inversion, the larger residues of U_{up}^* and U_e^* are distributed in two identical and symmetrical lobes. The orientation and shape of these lobes match with the true north component deformation pattern suggesting that these errors are intrinsically related to the removal of the north component. Even if the SVD-based approach shows also two lobes similarly oriented, these lobes are systematically asymmetrical (Fig. 7; Supplementary Material, Fig. S5). The lobe with the largest errors is actually located where no information on the north component was available during the inversion process and also where the residue of the north component is the largest (Fig. 7; Supplementary Material, Fig. S5). This observation suggests that even if the north component cannot be successfully retrieved during the truncated SVD because of the acquisition configuration (Fig. 7a; Supplementary Material, Fig. S5), it somehow brings an information that allows to partly reduce the errors in the east and vertical components. More generally, we observe that the errors become larger with two oblique incidence angles, errors that are also larger for U_{up}^* than U_e^* (Figs. 7 and Supplementary Material, Fig. S5). These tests confirm our previous observations: U_e^* is better retrieved than U_{up}^* using inversion-based decomposition methods.

Regarding the results obtained using the LC method, they show significant differences with the initial deformation field and with other approaches. Actually, not only the polarity of the signal differs from the original one but also the pattern. We highlight an asymmetry, different from that previously described for the SVD results, that is likely inherent to the way n_U and n_E are calculated. The asymmetry for U_{up}^* and the complexity of U_e^* tend to be reinforced as soon as the incidence angles capture more horizontal movement (Fig. 7 and Supplementary Material, Fig. S5). This method is supposed to be applied under

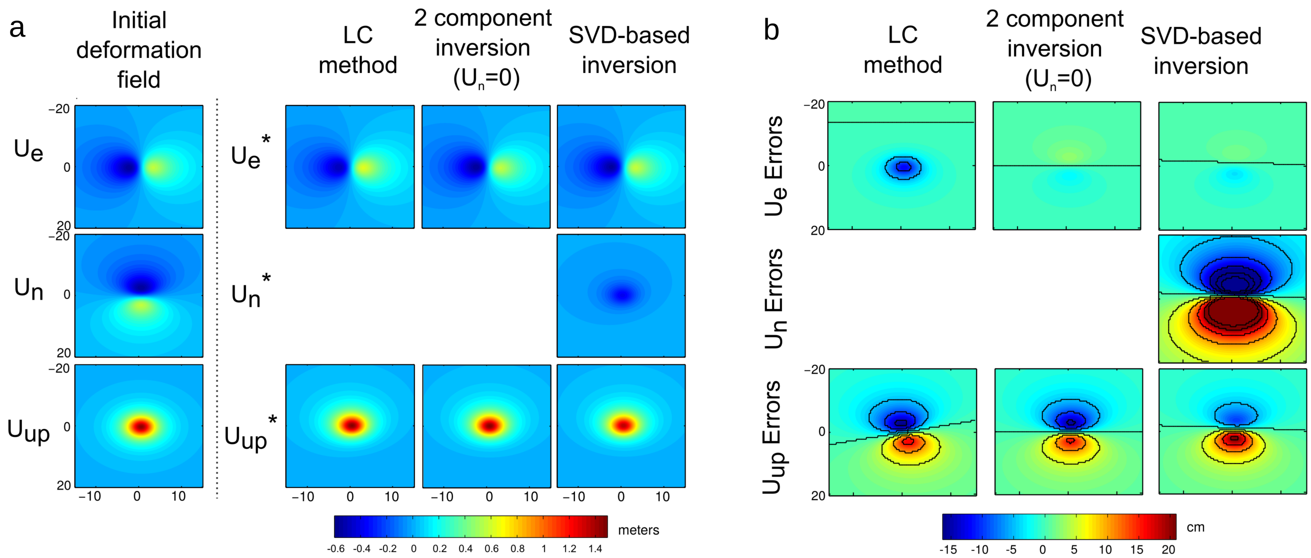

Figure 7. Comparison of decomposition results using synthetic data. (a) The first column shows the three space components of the *a priori* deformation field induced by a Mogi point source located at 4 km depth and associated with a volume change of 0.1 km^3. Synthetic ascending and descending interferograms were thus formed using CSK configuration (Table 1) and then decomposed. The next three columns show the results of the decomposition for each of the three methods presented in this study: the linear combination (LC), the two-component linear inversion associated with the hypothesis that U$_n$=0, and the SVD-based inversion (truncated SVD), our approach. (b) Comparison of the residuals obtained for the three decomposition methods. In b and d, the black lines represent error isolines every 5 cm. See Section 4.3.1 for more details and Supplementary Material, Figure S5 for complementary configurations.

specific conditions, including similar incidence angles; assumption that is not really met in the case of the CSK data presented in this study and also for those used in [De Zeeuw-van Dalfsen et al., 2012]. However, even with similar incidence angles, the differences appear significant, in particular for the pattern of U^*_{up} and for U^*_e whose residues are of the order of $1/5^e$ of the maximal east displacement (Supplementary Material, Fig. S5). The complex pattern is likely due to secondary contributions from the two other components that have not been fully removed by the linear combinations.

To complete this analysis, we performed a similar approach for three other classical processes inducing surface displacements: normal and strike-slip faulting as well as diking. This comparative analysis is presented using the cumulative errors calculated for each retrieved component, each decomposition method and each combination of incidence angle as presented in Figure 8. The highest cumulative error obtained among all decomposition methods, at fixed component and fixed geometry, was used for normalization. All the processes are characterized using their ratio of vertical to horizontal (east and north

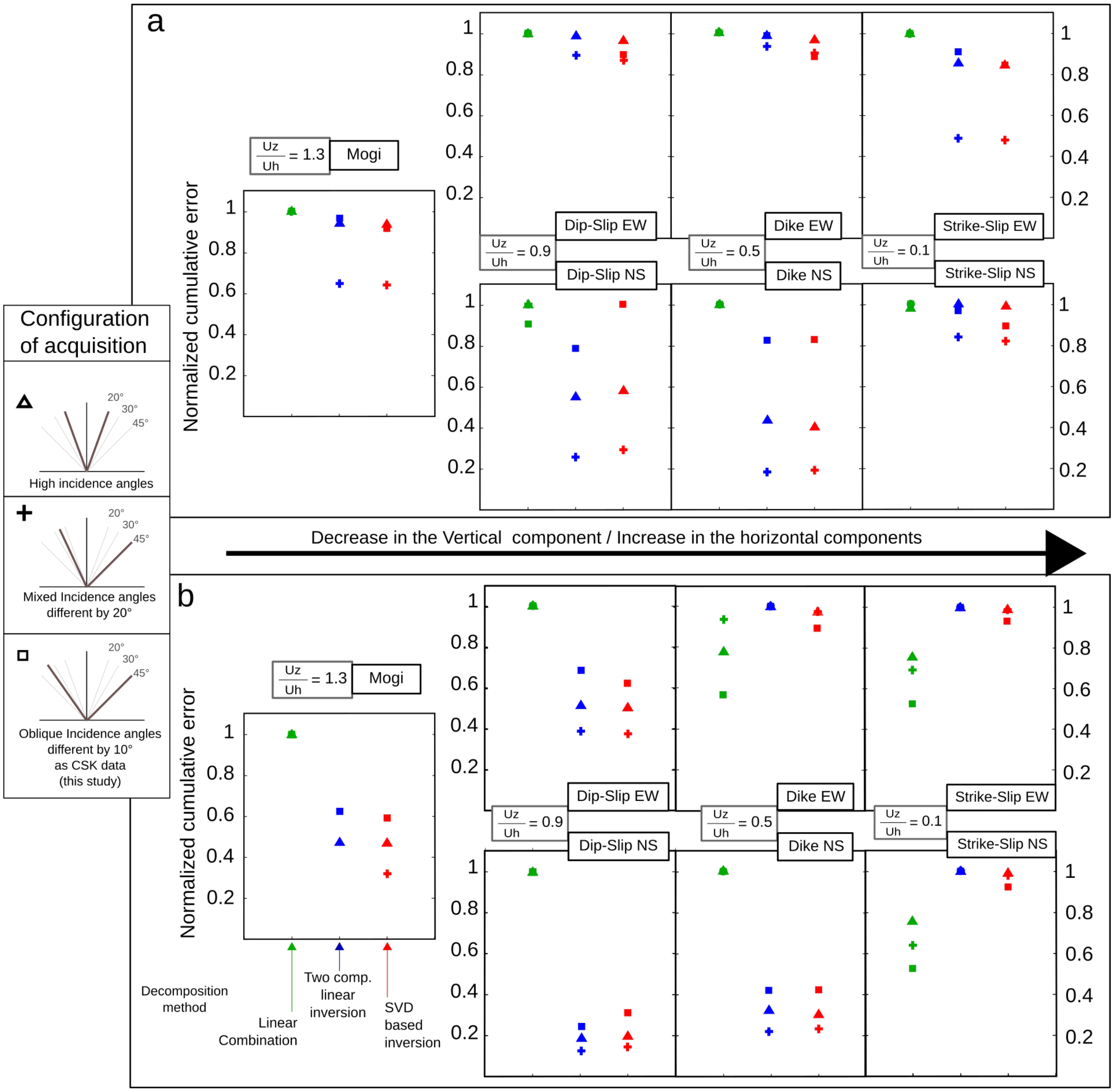

Figure 8. Comparison of decomposition results for classical models of deformation field and three combinations of incidences angles (symbols). Results are presented by their normalized cumulative errors for U^*_{up} (a) and U^*_e (b) and as a function of the U_z/U_h ratio. The color code indicates the decomposition method and the symbols correspond to a specific configuration of incidence angles. For oriented structures such faults and dikes, two end-member orientations were considered: East-West (upper panels) and North-South (lower panels). See Section 4.3.2 for discussion on oriented structures and their influence on reconstructed components.

373 components) displacements (U_z/U_h) in order to emphasize their impact on the reconstruction of U^*_{up} and
374 U^*_e. Similarly, we also test the influence of the combined incidence angles with respect to these different
375 deformation fields to see whether or not they differently impact the component retrieval. To do so, we

considered the three configurations presented in Figure 3: 1) two high incidence angles representing most of acquisitions with ERS-1/2 and ENVISAT satellites similarly as in [Keiding et al., 2010] and 2) mixed incidence angles represented by a high and an oblique incidence angles [Parks et al., 2018], and finally 3) two very oblique incidence angles, e.g $\backsim 30°$ illustrated with our CSK data set.

Starting with U^*_{up} (Fig. 8a), the maximal error is almost systematically detected for the LC method, whatever the combination of incidence angles. On the contrary, the two inversion-based decomposition methods result in very similar error behavior. These errors are slightly better than those for LC method but not much, except for north-south structure inducing both vertical and horizontal movements. Moreover, except for intermediate U_z/U_h ratio associated with north-south oriented structure, all errors for retrieving U^*_{up} remain significant, as most of them are $> 80\%$. When comparing the different geometries of acquisition, it clearly appears that errors in reconstructing U^*_{up} are minimized for mixed incidence angles, errors that are down to 25% for a north-south striking dyke. Finally, the differences between eastward and northward striking structures suggest that their orientation does influence the retrieval of the vertical component, which will be further discussed in the next section.

The distribution of U^*_e errors behave differently than those for U^*_{up} (Fig. 8b), even though the errors for the two inversion based methods are once more, very similar. The difference between the inversion-based methods and the LC one is more pronounced, $> 20\%$ in general, than for U^*_{up}. LC method shows largest errors when the deformation field is dominantly vertical or $U_z/U_h \sim 1$, whatever the configurations of acquisition. In other cases, the smallest errors are obtained for the two oblique incidence or mixed angles while the largest errors result from the two-component linear inversion, the SVD-based method being very closed but slightly inferior. As for U^*_{up}, clear differences appear in error distribution for northward and eastward structures confirming the impact of the structure orientation on the component reconstruction.

4.3.2 How oriented sources of deformation do influence decomposition results?

With Figure 8, the difference in error distribution of U^*_{up} and U^*_e for eastward and northward striking geological structures evidences how their retrieval depends on the deformation field and therefore the structure orientation. Whatever the structure azimuth, the retrieval of U^*_{up} is optimized using mixed incidence angles and the two inversion-based decomposition methods, the combination of two oblique incidence angles resulting in the largest errors. Conditions for optimizing U^*_e reconstruction are slightly different. For $U_z/U_h \sim 1$, mixed incidence angles combined with one inversion-based decomposition method provide best results, with limited errors on U^*_e. For very low U_z/U_h characterizing almost pure horizontal movement, LC method associated with two oblique incidence angles reduces errors by $\sim$20% when compared to other decomposition methods. For intermediate U_z/U_h ratio, the orientation of the structure should be taken into account to decide on the optimal decomposition method to retrieve U_e^*.

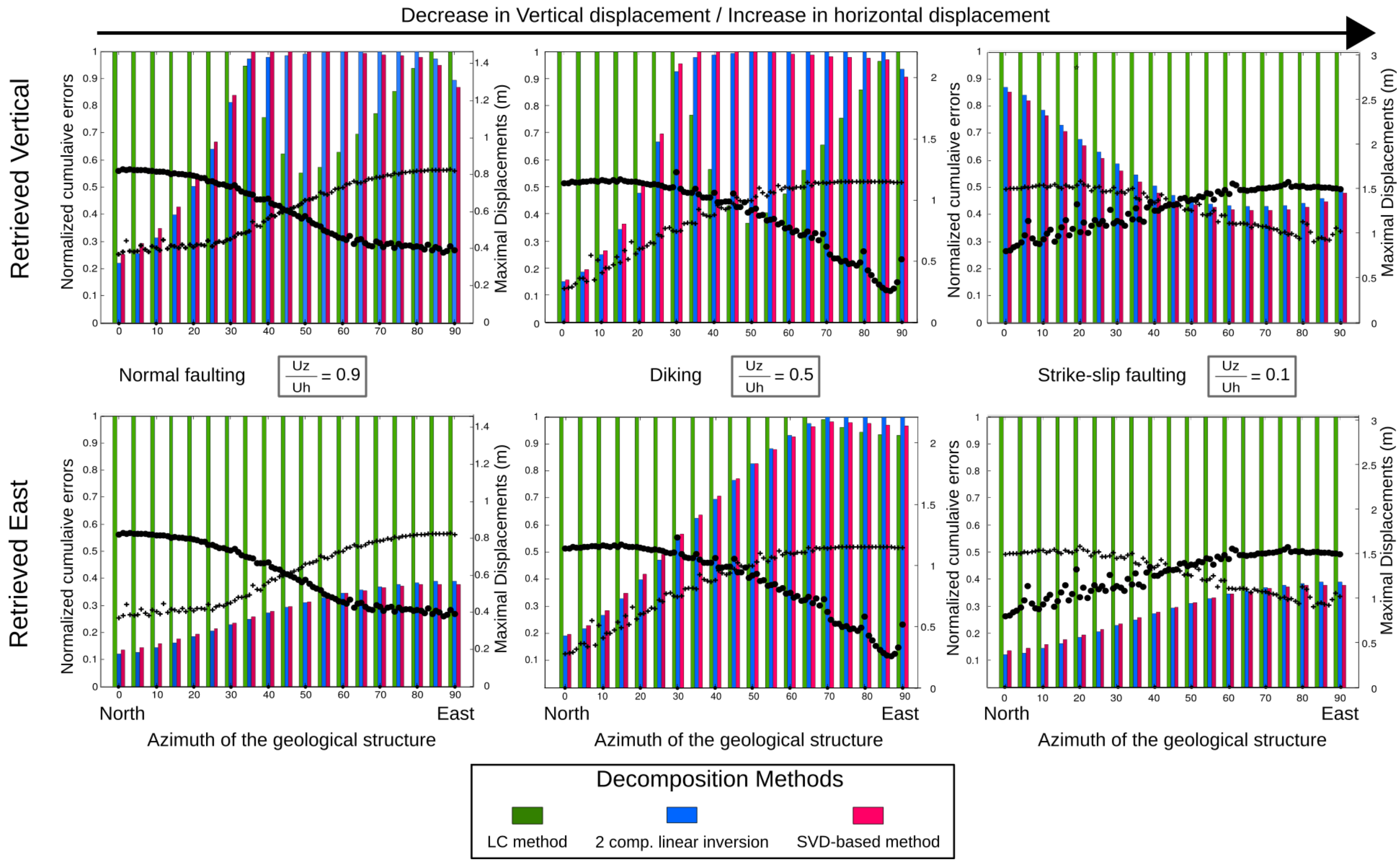

Figure 9. Sensivity of decomposition errors to structure orientation and horizontal displacement. The structure of geological structure (fault, dike) are taken from 0 (North) to 90° (East). For each strike, three coloured bars indicate the normalized cumulative errors of a decomposition method. The figure includes also maximal values of U_e (black filled circles) and U_n (black crosses) to better evaluate the correlation between the errors and the horizontal components of the deformation field.

We further investigate the influence of oriented structures on the retrieval on east and vertical components using similar sources of deformation as in Figure 8. We calculated the cumulative errors for strikes ranging from 0° (north-south) to 90° (east-west) for each structure and decomposition method and we fixed the combination of incidence angles to the mixed one (Fig. 9). If we consider only the error distribution in Fig. 9 (colored bars), three general observations may be done: 1) in most cases, the cumulative error distribution varies non-linearly with the strike of the geological structure and differently between U_{up}^* and U_e^*, 2) the cumulative errors are very similar for the two inversion-based methods and 3) the LC method is associated with most of the largest errors and especially, when dealing with a horizontal dominantly deformation field. Superimposing the vertical and horizontal displacements to the cumulative errors allows to decipher the source of these discrepancies (Fig. 9). For strike-slip faulting, the cumulative error of U_e^* for the two inversion-based methods is correlated with U_e and anticorrelated with U_n. The contrary trend is observed for U_{up}^* errors (Fig. 9). For structures inducing both vertical and horizontal movements, some common patterns appear in the error distribution. For U_{up}^* retrieval, as soon as $U_e > U_n$, the two-component linear inversion and SVD-based decomposition allow to significantly reduce the cumulative errors, what corresponds to strikes ranging from 0° to 30°. When U_e starts to be of the same order than U_n and smaller, LC methods show reduced errors. Regarding U_e^* retrieval, when $U_z/U_h \sim 1$, errors are minimized with the two inversion-based decompositions whose evolution with strike variations correlates with U_n. With increase of horizontal movements, these inversion-based decompositions provide the smaller errors up to 65°, after which the errors of the three methods differ by less than 10% (Fig. 9).

This analysis has shown that the distribution of cumulative errors depends on the distribution of horizontal displacements, and in particular those of the north component. This may be explained by the model resolution matrix (Fig. 3) and U_n representing systematically the second minor contributions to U_{up}^* and U_e^*, whatever the geometry of acquisition.

4.3.3 Modelling using the reconstructed components

With this section, we would like to take advantage of this comparison and more importantly of the model resolving matrix for testing modelling approaches. As we have seen in the past sections, model resolution matrix allows to quantify the ability to reconstruct the three components of the deformation field using the set of equations characterizing the combination of an ascending and a descending interferograms (Eq. 2). As LC method does not rely on the system of equations as defined in Eq. 2 as well as the two-component linear inversion as it modifies this initial system, it does not make sense to apply the model resolution matrix to both of these decomposition methods. Here our modelling approach consists in testing three modelling approaches (Supplementary Material, Fig. S6): 1) the classical one that consists first in projecting the modelled deformation field into the ascending and descending LOS to estimate the misfits in both configurations that are then summed up. 2) The second approach relies first on a decomposition of the ascending and descending interferograms using either the LC method or the two-component linear inversion to reconstruct U_{up}^* and U_e^*. These components are then compared to those of the modelled deformation field. 3) Similarly to the second approach, this last approach consists in decomposing the data into the three components of the deformation using the SVD-based inversion, even if U_n^* is not reliable. The misfit is then calculated using these components representing the observations, and those of the modelled deformation field once the model resolution matrix has been applied. This approach allows to substract comparable components, that are all seen through a SAR sensor. In the second and third approaches, the components obtained from modelling are considered as those of the true deformation field.

Our modelling procedure consists in a non-linear inverse problem we solve using a simulated annealing (Kirkpatrick *et al*, (1983); Kirkpatrick, 1984). The model parameters are sampled using a Markov chain combined to the Metropolis algorithm ([Metropolis et al., 1953], [Kirkpatrick, 1984]). This semi-random-walk is controlled by an external parameter called the "temperature" allowing to reconstruct the *a posteriori* probability of the model parameters. For each temperature, 300 iterations are performed. Here we test a Mogi point source with parameters similar as those in section 4.3.1 and interferograms simulated using the acquisition geometry of CSK data presented in this study (Table 1). The model parameters investigated during this inversion process are the volume change and the depth, the location being fixed (Fig. 10).
The four approaches led to parameter estimates for both the depth and volume change, that are very similar and very closed to the original ones. However, the use of model resolution matrix reduces significantly the uncertainties for both modelled parameters. It seems it also contributes to improve the inversion results as the best estimates are obtained using this approach (Fig. 10).

5 Discussion

Our comparison using an example from Iceland and synthetic data demonstrates that the choice of the method for decomposing InSAR signals impacts the reconstruction of the displacement components. More precisely, for a deformation field dominated by vertical motion, the SVD-based approach and the two-component linear inversion will result in very similar retrieved east and vertical displacements (Fig. 6; Fig. 7 and Supplementary Material). With increasing horizontal displacement, the differences between the three approaches become more and more pronounced, especially between the inversion-based methods and the LC method (Fig. 6; Fig. 7). When comparing the two inversion-based methods, it appears they give relatively similar results, with differences more or less pronounced depending on the combination of incidence angles/headings and the deformation field (Figs. 7, 9, 8 and Supplementary Material). Our approach also shows a minimum variation in range. This latter can reflect two processes or their combination: (1) the minimum length solution that is used by the SVD algorithm or/and (2) the consequence of the removal of the north component on U_e^* and U_{up}^* for the other approaches. Using the model resolution matrix (Fig. 3), we have shown that the true north component influences all the components of the reconstructed deformation field. U_n appears systematically as a secondary contribution to the reconstructed U_{up}^* and U_e^* components. Therefore assuming U_n is zero, will impact both U_{up}^* and U_e^* as suggested by [Samieie-Esfahany et al., 2009]. As the contribution of U_n is not the same for each reconstructed component of the deformation field, its removal affects differently the reconstruction of

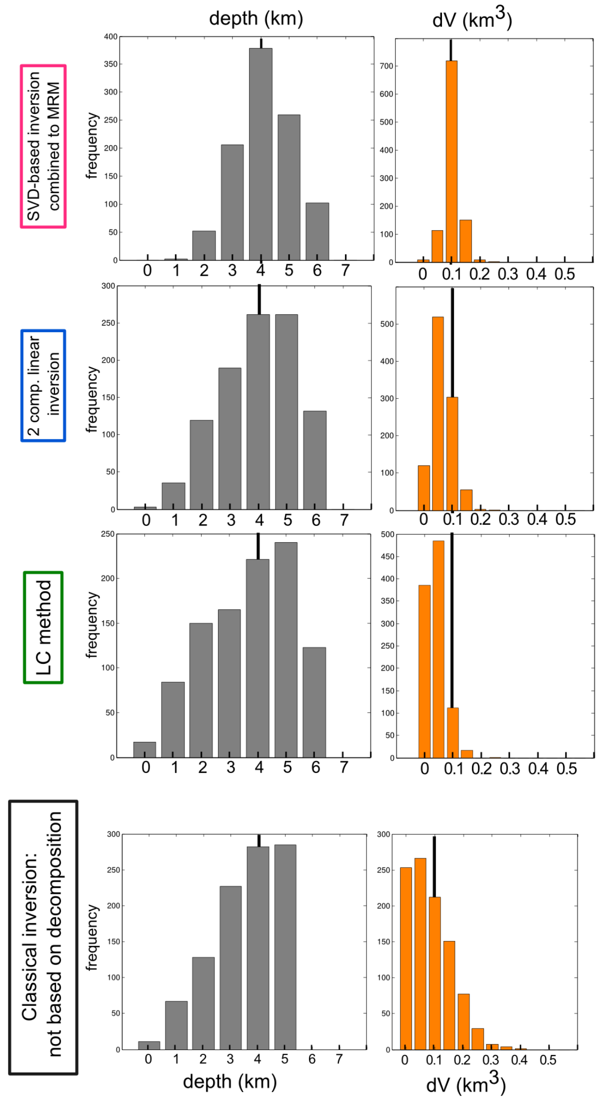

Figure 10. Modelling a deformation field using reconstructed components due to a Mogi source located a 4 km depth and dV=0.1 km^3. The *a-posteriori* probability for the depth and volume change parameters are shown in the first and second columns for each decomposition method, e.g LC method, two-component linear inversion and SVD-based inversion and the classical approach that relies only on LOS data. The black lines in the background represents the fixed model parameters. See Section 4.3.3 for more details.

the other components hence the differences observed between the two-component linear inversion to the truncated SVD (Fig. 6 and 7 and Supplementary Material). More, the SVD-based method will slightly improve the results with respect to the two-component linear inversion when different incidence angles will be considered (Fig. 7; Supplementary Material, Fig. S5).

Differences between truncated SVD and LC method can be explained using the equations 10 -11 that describe the LC method. They allow to estimate n_U and n_E considering empirical contributions of the true displacement components using assumptions that are usually only approximatively validated (see Section 3.1). Therefore the linear combinations of the LC method do not reflect the geometry of acquisition as the model resolution matrix does. Although contributions of the true components in the LC method are to first-order relatively similar as those of the model resolution matrix, the LC method does not allow to reconstruct the components of interest as well as the truncated SVD approach does as illustrated with synthetics (Fig. 7; Supplementary Material, Fig. S5).

Comparing different combinations of incidence angles for a same displacement field (see Section 4.3.1; Supplementary Material, Fig. S5) revealed that a decomposition method relying on data with highly oblique incidence angles does not improve the reconstruction of the east component and this, even if each individual interferogram shows a greater sensitivity to the east-oriented displacements. Actually, it is even worse as it reduces the sensitivity to the vertical displacements. These effects were already demonstrated by the model resolution matrix (Fig. 3). Actually, the east component is in essence well reconstructed by combining an ascending and a descending interferogram because of the orientation of the co-plane defined by the ascending and descending geometries (Fig. 1). In the light of these comparisons, it therefore seems preferable to combine interferograms with mixed or high incidence angles and similar look direction ($\mid \tilde{\alpha}_D \mid = \mid \tilde{\alpha}_A \mid$), whatever is the deformation field. More, the truncated SVD has shown to be the most reliable solution for retrieving U^*_{up} and U^*_e, in addition to present the advantage of limiting the *a priori* information on the displacement field to solve the system (2). The minimum length assumption used by the truncated SVD not only contributes to stabilize solutions, limiting extra variations due to *a priori* hypothesis on the deformation field, but also provides solutions consistent with natural processes whose energy is intrinsically minimized, making in that sense the SVD-based inversion better than the two others.

InSAR and therefore retrieved components from an InSAR pair, can provide high-resolution data in very high inaccessible areas as illustrated with Bárdarbunga example where high coherence measurements were obtained in between the glacier tongues (Fig. 5). These data brings valuable constrain on how surface deformation varies in space and potentially in time, depending on the ground conditions at the time of the next acquisition and offering therefore opportunity to better decipher the source of surface deformation and associated processes. Such information is particularly valuable when modelling the deformation source as more information are beneficial for converging towards the best solution, even more when several sources interact. With this study, our modelling approach has proven that model resolution matrix could improve the results and reduce the uncertainties when included in the misfit calculations. This approach is different from the classical one which consists in projecting the predicted deformation field into the ascending and/or descending LOS that are then compared to the original ascending and descending interferograms respectively for estimating the misfit. Such procedure implies that each interferogram contributes independently to the misfit, that represents a sum of all differences between the model and the interferograms. Our procedure in using the model resolution matrix allows to compare any deformation field as seen by ascending and descending satellite geometries, a somehow equivalent approach to the classical one but different in the sense that it does consider the information carried by all interferograms together.

Model resolution matrix could also be considered to explore the best configurations for deploying instruments in the field in order to get the best data possible for optimizing the inversion process (see [Bertero et al., 1985], [Bertero et al., 1988], [Jourde et al., 2015]). For satellite-based SAR sensors, the geometry of acquisition is pre-defined along near-polar orbits with only possible changes, e.g. in the incidence angle, except if the design of satellite system would be changed in the future. Therefore the model resolution matrix will not change dramatically from one configuration to another one, as we showed through our example from Iceland and those taken from the literature (Fig. 3). However, when InSAR data is combined with GNSS data, the model resolution matrix approach could be used to assess the optimal location for GNSS observations using a likely source of deformation. This would allow to better capture the ground movement and to optimize the inversion process of the three displacement components. Such analysis would be an extension to approaches based on inversion of three dimensional displacement fields combining InSAR and GNSS (e.g., [Gudmundsson et al., 2002]; [Wang et al., 2012]; [Pagli et al., 2014]).

6 Conclusion

Interferometric analysis of synthetic aperture radar satellite images allows to quantify the relative ground deformation between two SAR acquisitions. For an InSAR pair, one interferogram from a descending satellite pass and one from an ascending pass, the geometry of acquisition precludes full retrieval of the components of the three dimensional displacement field. The model resolution matrix allows to translate mathematically the filter imposed by the acquisition geometry of the satellites with SAR sensors on board and therefore to quantify our ability to reconstruct the deformation field with respect to the true one. This approach shows that all true components contribute to the reconstruction of all displacement components through different linear combinations, with a better reconstruction obtained for the east component than for the vertical one. We perform an inversion of the under-determined system defined by an InSAR pair, using a truncated Singular Value Decomposition and a minimum length solution. We compare our results with other methods classically used to retrieve the vertical and east components using an InSAR pair: the linear combination (LC) method and the two-component linear inversion. The comparison is performed using a real example taken from the 2014-2015 volcano-tectonic event in Iceland but also synthetics and modelling. We thus analyze different deformation fields and show that the largest errors are generally obtained for the LC method, while our SVD-based approach and the two-component linear inversion result in relatively similar estimates. These results are further examined with respect to the configuration of acquisition of the two interferograms combined, the nature of the deformation field and orientation of the geological structures. They suggest in particular that combining two interferograms with both high or mixed incidence angles allow a better reconstruction of the east and vertical components than having two oblique incidence angles. Finally, we show that the model resolution matrix can be used in combination with retrieved displacement components to better constrain an inverse problem that aims at solving source parameters of a deformation field.

7 Acknowledgement

This work was performed during a postdoctoral fellowship supported by the European Community's Seventh Framework Programme Grant No. 308377 (Project FUTUREVOLC). SD is currently supported by the FCT postdoctoral grant (SFRH/BPD/17714/2016). An intermediate TanDEM-X digital elevation model was provided by DLR under project IDEM_GEOL0123. COSMO-SkyMed data were provided by the Italian Space Agency (ASI) and TerraSAR-X data by the German Space Agency (DLR) through the Icelandic Volcanoes Supersite project supported by the Committee on Earth Observing Satellites (CEOS).

References

[Bechor and Zebker, 2006] Bechor, N. B. D. and Zebker, H. A. (2006). Measuring two-dimensional movements using a single InSAR pair. *Geophysical Research Letters*, 33(16):1–5.

[Béjar-Pizarro et al., 2017] Béjar-Pizarro, M., Notti, D., Mateos, R. M., Ezquerro, P., Centolanza, G., Herrera, G., Bru, G., Sanabria, M., Solari, L., Duro, J., et al. (2017). Mapping vulnerable urban areas affected by slow-moving landslides using sentinel-1 insar data. *Remote Sensing*, 9(9):876.

[Bell et al., 2008] Bell, J. W., Amelung, F., Ferretti, A., Bianchi, M., and Novali, F. (2008). Permanent scatterer insar reveals seasonal and long-term aquifer-system response to groundwater pumping and artificial recharge. *Water Resources Research*, 44(2).

[Bertero et al., 1985] Bertero, M., De Mol, C., and Pike, E. R. (1985). Linear inverse problems with discrete data. i. general formulation and singular system analysis. *Inverse problems*, 1(4):301.

[Bertero et al., 1988] Bertero, M., De Mol, C., and Pike, E. R. (1988). Linear inverse problems with discrete data: Ii. stability and regularisation. *Inverse problems*, 4(3):573.

[Casu et al., 2006] Casu, F., Manzo, M., and Lanari, R. (2006). A quantitative assessment of the SBAS algorithm performance for surface deformation retrieval from DInSAR data. *Remote Sensing of Environment*, 102(3-4):195–210.

[Cavalié et al., 2008] Cavalié, O., Lasserre, C., Doin, M.-P., Peltzer, G., Sun, J., Xu, X., and Shen, Z.-K. (2008). Measurement of interseismic strain across the haiyuan fault (gansu, china), by insar. *Earth and Planetary Science Letters*, 275(3-4):246–257.

[Chaussard, 2016] Chaussard, E. (2016). Subsidence in the Pari cutin lava field: Causes and implications for interpretation of deformation fields at volcanoes. *Journal of Volcanology and Geothermal Research*, 320:1–11.

[Chaussard et al., 2013] Chaussard, E., Amelung, F., Abidin, H., and Hong, S. H. (2013). Sinking cities in Indonesia: ALOS PALSAR detects rapid subsidence due to groundwater and gas extraction. *Remote Sensing of Environment*, 128:150–161.

[Chaussard et al., 2014] Chaussard, E., Wdowinski, S., Cabral-Cano, E., and Amelung, F. (2014). Land subsidence in central Mexico detected by ALOS InSAR time-series. *Remote Sensing of Environment*, 140:94–106.

[Chen and Zebker, 2002] Chen, C. W. and Zebker, H. A. (2002). Phase unwrapping for large sar interferograms: Statistical segmentation and generalized network models. *IEEE Transactions on Geoscience and Remote Sensing*, 40(8):1709–1719.

[Coppola et al., 2017] Coppola, D., Ripepe, M., Laiolo, M., and Cigolini, C. (2017). Modelling satellite-derived magma discharge to explain caldera collapse. *Geology*, 45(6):523–526.

[De Zeeuw-van Dalfsen et al., 2012] De Zeeuw-van Dalfsen, E., Pedersen, R., Hooper, A., and Sigmundsson, F. (2012). Subsidence of Askja caldera 2000-2009: Modelling of deformation processes at an extensional plate boundary, constrained by time series InSAR analysis. *Journal of Volcanology and Geothermal Research*, 213-214:72–82.

[Drouin and Sigmundsson, 2019] Drouin, V. and Sigmundsson, F. (2019). Countrywide observations of plate spreading and glacial isostatic adjustment in iceland inferred by sentinel-1 radar interferometry, 2015–2018. *Geophysical Research Letters*, 46(14):8046–8055.

[Drouin et al., 2017] Drouin, V., Sigmundsson, F., Verhagen, S., Ófeigsson, B. G., Spaans, K., and Hreinsdóttir, S. (2017). Deformation at krafla and bjarnarflag geothermal areas, northern volcanic zone of iceland, 1993–2015. *Journal of Volcanology and Geothermal Research*, 344:92–105.

[Dumont et al., 2018] Dumont, S., Sigmundsson, F., Parks, M. M., Drouin, V. J., Pedersen, G., Jónsdóttir, I., Höskuldsson, Á., Hooper, A., Spaans, K., Bagnardi, M., et al. (2018). Integration of sar data into monitoring of the 2014-2015 holuhraun eruption, iceland: Contribution of the icelandic volcanoes supersite and the futurevolc projects. *Frontiers in Earth Science*, 6:231.

[Dumont et al., 2016] Dumont, S., Socquet, A., Grandin, R., Doubre, C., and Klinger, Y. (2016). Surface displacements on faults triggered by slow magma transfers between dyke injections in the 2005-2010 rifting episode at Dabbahu-Manda-Hararo rift (Afar, Ethiopia). *Geophysical Journal International*, 204(1):399–417.

[ElGharbawi and Tamura, 2015] ElGharbawi, T. and Tamura, M. (2015). Coseismic and postseismic deformation estimation of the 2011 Tohoku earthquake in Kanto Region, Japan, using InSAR time series analysis and GPS. *Remote Sensing of Environment*, 168:374–387.

[Fialko et al., 2001] Fialko, Y., Simons, M., and Agnew, D. (2001). The complete (3-d) surface displacement field in the epicentral area of the 1999 mw7. 1 hector mine earthquake, california, from space geodetic observations. *Geophysical Research Letters*, 28(16):3063–3066.

[Froger et al., 2004] Froger, J.-L., Fukushima, Y., Briole, P., Staudacher, T., Souriot, T., and Villeneuve, N. (2004). The deformation field of the august 2003 eruption at piton de la fournaise, reunion island, mapped by asar interferometry. *Geophysical research letters*, 31(14).

[Fujiwara et al., 2000] Fujiwara, S., Nishimura, T., Murakami, M., Nakagawa, H., Tobita, M., and Rosen, P. A. (2000). 2.5-d surface deformation of m6. 1 earthquake near mt iwate detected by sar interferometry. *Geophysical research letters*, 27(14):2049–2052.

[Gabriel et al., 1989] Gabriel, A. K., Goldstein, R. M., and Zebker, H. A. (1989). Mapping small elevation changes over large areas: differential radar interferometry. *Journal of Geophysical Research: Solid Earth*, 94(B7):9183–9191.

[Goldstein and Werner, 1998] Goldstein, R. M. and Werner, C. L. (1998). Radar interferogram filtering for geophysical applications. *Geophysical research letters*, 25(21):4035–4038.

[Golub and Kahan, 1965] Golub, G. and Kahan, W. (1965). Calculating the singular values and pseudo-inverse of a matrix. *Journal of the Society for Industrial and Applied Mathematics, Series B: Numerical Analysis*, 2(2):205–224.

[Gudmundsson et al., 2016] Gudmundsson, M. T., Jónsdóttir, K., Hooper, A., Holohan, E. P., Halldórsson, S. A., Ófeigsson, B. G., Cesca, S., Vogfjörd, K. S., Sigmundsson, F., Högnadóttir, T., et al. (2016). Gradual caldera collapse at bárdarbunga volcano, iceland, regulated by lateral magma outflow. *Science*, 353(6296):aaf8988.

[Gudmundsson et al., 2002] Gudmundsson, S., Sigmundsson, F., and Carstensen, J. M. (2002). Three-dimensional surface motion maps estimated from combined interferometric synthetic aperture radar and gps data. *Journal of Geophysical Research: Solid Earth*, 107(B10).

[Hansen et al., 1992] Hansen, P. C., Sekii, T., and Shibahashi, H. (1992). The modified truncated svd method for regularization in general form. *SIAM Journal on Scientific and Statistical Computing*, 13(5):1142–1150.

[Hanssen, 2001] Hanssen, R. F. (2001). *Radar interferometry: data interpretation and error analysis*, volume 2. Springer.

[Heimisson and Segall, 2020] Heimisson, E. R. and Segall, P. (2020). Physically consistent modeling of dike induced deformation and seismicity: Application to the 2014 bárðarbunga dike, iceland. *Journal of Geophysical Research: Solid Earth*, 125:e2019JB018141.

[Hu et al., 2014] Hu, J., Li, Z. W., Ding, X. L., Zhu, J. J., Zhang, L., and Sun, Q. (2014). Resolving three-dimensional surface displacements from InSAR measurements: A review. *Earth-Science Reviews*, 133(June):1–17.

[Hutchison et al., 2016] Hutchison, W., Biggs, J., Mather, T. A., Pyle, D. M., Lewi, E., Yirgu, G., Caliro, S., Chiodini, G., Clor, L. E., and Fischer, T. P. (2016). Causes of unrest at silicic calderas in the east african rift: New constraints from insar and soil-gas chemistry at aluto volcano, ethiopia. *Geochemistry, Geophysics, Geosystems*, 17(8):3008–3030.

[Jo et al., 2015] Jo, M.-J., Jung, H.-S., Won, J.-S., and Lundgren, P. (2015). Measurement of three-dimensional surface deformation by cosmo-skymed x-band radar interferometry: Application to the march 2011 kamoamoa fissure eruption, kīlauea volcano, hawai'i. *Remote Sensing of Environment*, 169:176–191.

[Johannesson and Saemundsson, 2009] Johannesson, H. and Saemundsson, K. (2009). Geological map of iceland, tectonics 1:600.000.

[Joughin et al., 1998] Joughin, I. R., Kwok, R., and Fahnestock, M. A. (1998). Interferometric estimation of three-dimensional ice-flow using ascending and descending passes. *IEEE Transactions on Geoscience and Remote Sensing*, 36(1):25–37.

[Jourde et al., 2015] Jourde, K., Gibert, D., and Marteau, J. (2015). Improvement of density models of geological structures by fusion of gravity data and cosmic muon radiographies. *Geoscientific Instrumentation, Methods and Data Systems*, 4(2):177.

[Keiding et al., 2010] Keiding, M., Árnadóttir, T., Jonsson, S., Decriem, J., and Hooper, A. (2010). Plate boundary deformation and man-made subsidence around geothermal fields on the reykjanes peninsula, iceland. *Journal of Volcanology and Geothermal Research*, 194(4):139–149.

[Kirkpatrick, 1984] Kirkpatrick, S. (1984). Optimization by simulated annealing: Quantitative studies. *Journal of statistical physics*, 34(5-6):975–986.

[Kumar et al., 2011] Kumar, V., Venkataramana, G., and Høgda, K. A. (2011). Glacier surface velocity estimation using sar interferometry technique applying ascending and descending passes in himalayas. *International Journal of Applied Earth Observation and Geoinformation*, 13(4):545–551.

[Lundgren et al., 2004] Lundgren, P., Casu, F., Manzo, M., Pepe, A., Berardino, P., Sansosti, E., and Lanari, R. (2004). Gravity and magma induced spreading of mount etna volcano revealed by satellite radar interferometry. *Geophysical Research Letters*, 31(4).

[Magnússon et al., 2005] Magnússon, E., Björnsson, H., Dall, J., and Pálsson, F. (2005). Volume changes of vatnajökull ice cap, iceland, due to surface mass balance, ice flow, and subglacial melting at geothermal areas. *Geophysical Research Letters*, 32(5).

[Manzo et al., 2006] Manzo, M., Ricciardi, G., Casu, F., Ventura, G., Zeni, G., Borgström, S., Berardino, P., Del Gaudio, C., and Lanari, R. (2006). Surface deformation analysis in the ischia island (italy) based on spaceborne radar interferometry. *Journal of Volcanology and Geothermal Research*, 151(4):399–416.

[Massonnet and Feigl, 1998] Massonnet, D. and Feigl, K. L. (1998). Radar interferometry and its application to changes in the earth's surface. *Reviews of geophysics*, 36(4):441–500.

[Menke, 2018] Menke, W. (2018). *Geophysical data analysis: Discrete inverse theory*. Academic press.

[Metropolis et al., 1953] Metropolis, N., Rosenbluth, A. W., Rosenbluth, M. N., Teller, A. H., and Teller, E. (1953). Equation of state calculations by fast computing machines. *The journal of chemical physics*, 21(6):1087–1092.

[Mogi, 1958] Mogi, K. (1958). Relations between the eruptions of various volcanoes and the deformation of the ground surfaces around them. *Bull. Earthquake Res. Inst., Univ. Tokyo*, 36:99–134.

[Oelke and Zhang, 2004] Oelke, C. and Zhang, T. (2004). A model study of circum-arctic soil temperatures. *Permafrost and Periglacial Processes*, 15(2):103–121.

[Ozawa and Ueda, 2011] Ozawa, T. and Ueda, H. (2011). Advanced interferometric synthetic aperture radar (insar) time series analysis using interferograms of multiple-orbit tracks: A case study on miyake-jima. *Journal of Geophysical Research: Solid Earth*, 116(B12).

[Pagli et al., 2014] Pagli, C., Wang, H., Wright, T. J., Calais, E., and Lewi, E. (2014). Current plate boundary deformation of the afar rift from a 3-d velocity field inversion of insar and gps. *Journal of Geophysical Research: Solid Earth*, 119(11):8562–8575.

[Parker et al., 2016] Parker, A. L., Biggs, J., and Lu, Z. (2016). Time-scale and mechanism of subsidence at lassen volcanic center, ca, from insar. *Journal of Volcanology and Geothermal Research*, 320:117–127.

[Parks et al., 2018] Parks, M., Sigmundsson, F., Sigurðsson, Ó., Hooper, A., Hreinsdóttir, S., Ófeigsson, B., and Michalczewska, K. (2018). Deformation due to geothermal exploitation at reykjanes, iceland. *Journal of Volcanology and Geothermal Research*.

[Parks et al., 2017] Parks, M. M., Heimisson, E. R., Sigmundsson, F., Hooper, A., Vogfjörd, K. S., Árnadóttir, T., Ófeigsson, B., Hreinsdóttir, S., Hjartardóttir, Á. R., Einarsson, P., et al. (2017). Evolution of deformation and stress changes during the caldera collapse and dyking at bárdarbunga, 2014–2015: Implication for triggering of seismicity at nearby tungnafellsjökull volcano. *Earth and Planetary Science Letters*, 462:212–223.

[Pedersen et al., 2017] Pedersen, G., Höskuldsson, A., Dürig, T., Thordarson, T., Jonsdottir, I., Riishuus, M. S., Óskarsson, B. V., Dumont, S., Magnússon, E., Gudmundsson, M. T., et al. (2017). Lava field evolution and emplacement dynamics of the 2014–2015 basaltic fissure eruption at holuhraun, iceland. *Journal of Volcanology and Geothermal Research*, 340:155–169.

[Pinel et al., 2014] Pinel, V., Poland, M. P., and Hooper, A. (2014). Volcanology: Lessons learned from synthetic aperture radar imagery. *Journal of Volcanology and Geothermal Research*, 289:81–113.

[Riel et al., 2015] Riel, B., Milillo, P., Simons, M., Lundgren, P., Kanamori, H., and Samsonov, S. (2015). The collapse of bárðarbunga caldera, iceland. *Geophysical Journal International*, 202(1):446–453.

[Rosen et al., 2012] Rosen, P. A., Gurrola, E., Sacco, G. F., and Zebker, H. (2012). The insar scientific computing environment. In *Synthetic Aperture Radar, 2012. EUSAR. 9th European Conference on*, pages 730–733. VDE.

[Rucci et al., 2013] Rucci, A., Vasco, D., and Novali, F. (2013). Monitoring the geologic storage of carbon dioxide using multicomponent sar interferometry. *Geophysical Journal International*, 193(1):197–208.

[Ruch et al., 2016] Ruch, J., Wang, T., Xu, W., Hensch, M., and Jónsson, S. (2016). Oblique rift opening revealed by reoccurring magma injection in central iceland. *Nature communications*, 7:12352.

[Samieie-Esfahany et al., 2009] Samieie-Esfahany, S., Hanssen, R., van Thienen-Visser, K., and Muntendam-Bos, A. (2009). On the effect of horizontal deformation on insar subsidence estimates. In *Proceedings of The Fringe 2009 Workshop, Frascati, Italy*, volume 30.

[Samsonov et al., 2014] Samsonov, S. V., d'Oreye, N., González, P. J., Tiampo, K. F., Ertolahti, L., and Clague, J. J. (2014). Rapidly accelerating subsidence in the greater vancouver region from two decades of ers-envisat-radarsat-2 dinsar measurements. *Remote sensing of environment*, 143:180–191.

[Sigmundsson et al., 2015] Sigmundsson, F., Hooper, A., Hreinsdóttir, S., Vogfjörd, K. S., Ófeigsson, B. G., Heimisson, E. R., Dumont, S., Parks, M., Spaans, K., Gudmundsson, G. B., et al. (2015). Segmented lateral dyke growth in a rifting event at bárðarbunga volcanic system, iceland. *Nature*, 517(7533):191.

[Sun et al., 2017] Sun, H., Zhang, Q., Zhao, C., Yang, C., Sun, Q., and Chen, W. (2017). Monitoring land subsidence in the southern part of the lower liaohe plain, china with a multi-track ps-insar technique. *Remote Sensing of Environment*, 188:73–84.

[Tong and Schmidt, 2016] Tong, X. and Schmidt, D. (2016). Active movement of the cascade landslide complex in washington from a coherence-based insar time series method. *Remote Sensing of Environment*, 186:405–415.

[Vilardo et al., 2010] Vilardo, G., Isaia, R., Ventura, G., De Martino, P., and Terranova, C. (2010). Insar permanent scatterer analysis reveals fault re-activation during inflation and deflation episodes at campi flegrei caldera. *Remote Sensing of Environment*, 114(10):2373–2383.

[Wang et al., 2012] Wang, H., Wright, T. J., Yu, Y., Lin, H., Jiang, L., Li, C., and Qiu, G. (2012). Insar reveals coastal subsidence in the pearl river delta, china. *Geophysical Journal International*, 191(3):1119–1128.

[Wang et al., 2019] Wang, X., Aoki, Y., and Chen, J. (2019). Surface deformation of asama volcano, japan, detected by time series insar combining persistent and distributed scatterers, 2014–2018. *Earth, Planets and Space*, 71(1):1–16.

[Wang et al., 2014] Wang, X., Liu, G., Yu, B., Dai, K., Zhang, R., Chen, Q., and Li, Z. (2014). 3d coseismic deformations and source parameters of the 2010 yushu earthquake (china) inferred from dinsar and multiple-aperture insar measurements. *Remote sensing of environment*, 152:174–189.

[Wittmann et al., 2017] Wittmann, W., Sigmundsson, F., Dumont, S., and Lavallée, Y. (2017). Post-emplacement cooling and contraction of lava flows: Insar observations and a thermal model for lava fields at hekla volcano, iceland. *Journal of Geophysical Research: Solid Earth*, 122(2):946–965.

[Wright et al., 2004] Wright, T. J., Parsons, B. E., and Lu, Z. (2004). Toward mapping surface deformation in three dimensions using insar. *Geophysical Research Letters*, 31(1).